JOURNAL OF THERMOPHYSICS AND HEAT TRANSFER
Vol. 18, No. 1, January–March 2004

Combined Radiation–Conduction Analysis and Experiment of Ceramic Insulation for Reentry Vehicles

Toshiya Nakamura* and Takashi Kai†
National Aerospace Laboratory of Japan, Tokyo 181-0015, Japan

A finite element code for the transient combined radiation–conduction analysis is developed. The Gaussian quadratures technique and linear trial functions are used to approximate the scattering integration and the radiation intensity distribution, respectively. The Galerkin method is employed to yield a finite element formulation for radiation analysis. Numerical examples are presented and are compared with published solutions. It is found that the present code is equivalent to the other methods. A series of experiments with ceramic tile insulation is also conducted to examine the validity of the developed code. The transient temperature and the radiative heat flux at the back surface are measured during heating. Agreement is good between the experimental and the analytical results.

Nomenclature

c	=	specific heat, J/kg · K
I	=	radiation intensity, W/m^2 · sr
I_b	=	black body intensity function, W/m^2 · sr
I_{ir}	=	external irradiation intensity, W/m^2 · sr
K_e	=	extinction coefficient, m^{-1}
L	=	specimen thickness, m
n	=	refractive index
Q_{ir}	=	irradiation heat flux, W/m^2
Q_r	=	radiative heat flux at the back surface, W/m^2
T	=	absolute temperature, K
x	=	spatial coordinate, m
ϵ	=	emissivity
λ_s	=	solid conductivity, W/m · K
μ	=	direction cosine of polar angle
ρ	=	density, kg/m^3
ρ_i	=	reflectivity to incident from inside the material
ρ_o	=	reflectivity to incident from outside the material
σ	=	Stefan–Boltzmann constant, 5.67×10^{-8} W/m^2 · K^4
ω	=	albedo of scattering

Introduction

THE thermal protection system (TPS) is one of the most important parts in the structure design of a reentry vehicle. The guarded hot plate (GHP) method is usually used to measure the thermal conductivities of TPS materials that are used in engineering thermal/structural analyses. In the GHP method, there is a temperature gradient of roughly 1 K/1 mm thickness in the material. However, this temperature gradient is very small compared with that in the actual reentry flight where temperature gradient of about 1000 K per several centimeters can take place. Another characteristics of the GHP method is that it is static, although transient or dynamic analysis is always required in reentry phase. Another method to determine thermal conductivity is a transient technique in which the conductivity is estimated from the measured transient temperature responses. However, the obtained values do not coincide with the GHP data.[1,2]

Received 10 June 2003; revision received 29 July 2003; accepted for publication 30 July 2003.

*Senior Researcher, Flight Loads Group, Structures and Materials Research Center, 6-13-1, Osawa, Mitaka; nakamura.toshiya@jaxa.jp.

†Group Leader, Flight Loads Group, Structures and Materials Research Center, 6-13-1, Osawa, Mitaka. Member AIAA.

The heat transfer mechanism in a fibrous and highly porous insulation is a combination of the solid conduction, radiative heat transfer inside the material, and the effect of gas (air) in the material. Among them, the radiative heat transfer is dominant at high temperature. Many efforts have been made since the 1970s to model the effective thermal conductivity based on these heat transfer mechanisms.[3–6]

Schmitt et al. discussed the steady and transient effective thermal conductivity of reusable surface insulation based on the two-flux method.[7] Recently Marschall et al. investigated the role of internal radiation heat transfer as a possible cause for the differences between static and dynamic effective thermal conductivities using a simple, coupled, one-dimensional radiation–conduction model.[8] A micromechanism-based approach was presented by Tong and Tien[9] and Tong et al.[10] to discuss the radiative heat transfer in fibrous insulations based on the two-flux method. On the other hand, transient combined radiation and conduction heat transfer analyses have been reported in Refs. 11–16, for example.

Such mechanism-based approaches are important, not only for the advanced analysis of existing TPS with a ceramic tile, but also for the development of a metallic TPS. Blosser used the effective thermal conductivity in his thermal analysis of metallic TPS,[17] but recently Daryabeigi employed the combined analysis in his investigation of the heat transfer mechanism[11] and in the design analysis[12] of fibrous insulation.

Based on the preceding background and engineering needs, the authors are developing a finite element code that can incorporate the internal radiation into routine engineering thermal analyses of TPS. The objectives of the present study are to develop a basic one-dimensional code and to examine its fundamental validity through comparisons with experimental data. Transient temperatures and the radiative heat flux during rising temperature are measured where the latter directly reflects the combination of internal radiation and conduction. Analytical results are compared with the experimental data to examine the developed code.

Finite Element Analysis Code

Formulation

Although detailed radiative properties, such as spectral characteristics, anisotropy, and temperature dependencies, are discussed in the literature,[7,8,11,13,18] they are assumed to be gray, isotropic, and constant for simplicity in the present code.

The basic equations of radiation intensity and temperature for a gray, absorbing, emitting, and isotropically scattering medium with a one-dimension assumption are as follows:

$$\frac{\mu}{K_e}\frac{\partial I(x,\mu)}{\partial x} = -I(x,\mu) + \frac{\omega}{2}\int_{-1}^{1} I(x,\mu')\,\mathrm{d}\mu' + (1-\omega)n^2 I_b[T(x)] \tag{1}$$

Table 1 Comparison of the transient temperature distribution at $\xi = 0.05$ for several wall reflectivity cases[a]

Boundary conditions					Temperature distribution		
ϵ_1	ρ_1	ϵ_2	ρ_2	Investigators	$\tau = 0.25$	$\tau = 0.5$	$\tau = 0.75$
1	0	1	0	Lii and Ozisik[b]	0.4617	0.1474	0.0277
1	0	1	0	Sutton[c]	0.4888	0.1778	0.0591
1	0	1	0	Barker and Sutton[d]	0.4893	0.1775	0.0588
1	0	1	0	Tsai and Lin[e]	0.4889	0.1773	0.0588
1	0	1	0	Present	0.4889	0.1768	0.0582
1	0	0	1	Lii and Ozisik[b]	0.4716	0.1630	0.0545
1	0	0	1	Sutton[c]	0.5030	0.2005	0.0833
1	0	0	1	Barker and Sutton[d]	0.5035	0.2003	0.0831
1	0	0	1	Tsai and Lin[e]	0.5031	0.2001	0.0830
1	0	0	1	Present	0.5054	0.2034	0.0872
0.5	0.5	0.5	0.5	Lii and Ozisik[b]	0.4323	0.1196	0.0195
0.5	0.5	0.5	0.5	Sutton[c]	0.4671	0.1591	0.0499
0.5	0.5	0.5	0.5	Barker and Sutton[d]	0.4675	0.1587	0.0496
0.5	0.5	0.5	0.5	Tsai and Lin[e]	0.4671	0.1585	0.0495
0.5	0.5	0.5	0.5	Present	0.4668	0.1583	0.0500

[a]Where $\tau_0 = 1$, $\theta_1 = 1$, $\theta_2 = 0$, $\theta_0 = 0$, $\omega = 0.5$, and $\nu = 0.1$.
[b]Normal-mode expansion.[14]
[c]Hybrid Galerkin.[15]
[d]Integral transform technique.[16]
[e]Finite difference/nodal approximation.[13]

$$\rho c \frac{\partial T}{\partial t} = \frac{\partial}{\partial x}\left(\lambda_s \frac{\partial T}{\partial x} - q_r\right) \tag{2}$$

$$q_r(x) = 2\pi \int_{-1}^{1} \mu I(x, \mu)\, \mathrm{d}\mu \tag{3}$$

where q_r is the radiative heat flux.

In consideration of the potential for future extensions, a finite element method was employed. Roux et al. presented a finite element (FE) formulation of the radiative transfer equation based on the Galerkin method and discussed an application to fibrous insulation.[19] The authors followed the similar formulation, which is briefly described here. The ordinary FE program for one-dimensional heat conduction was then combined with this FE code for radiation.

The Gauss–Legendre integration technique was used to approximate the scattering integration in Eq. (1) as follows:

$$\int_{-1}^{1} I(x, \mu')\, \mathrm{d}\mu' \approx \sum_{l=1}^{M} w_l I(x)_l \tag{4}$$

where $I(x)_l = I(x, \mu_l)$. Here w_l and $\mu_l, l = 1, \ldots, M$, are the weights and the roots of the Legendre polynomials, respectively. Linear trial functions $N_1(x)$ and $N_2(x)$ are used to approximate the radiation intensity in each element as follows:

$$I^e(x, \mu_l) = I^e(x)_l = \sum_{n=1}^{2} I^e_{nl} N_n(x) \tag{5}$$

$$N_1(x) = \left(x_2^e - x\right) \Big/ \left(x_2^e - x_1^e\right), \qquad N_2(x) = \left(x - x_1^e\right) \Big/ \left(x_2^e - x_1^e\right) \tag{6}$$

where $I^e_{nl} = I(x^e_n, \mu_l)$ and the superscript e denotes the value defined within an element that is bounded by the nodes x_1^e and x_2^e, where $x_1^e \le x \le x_2^e$. By substituting Eqs. (4) and (5) for Eq. (1), we have the residual. Then, applying the Galerkin method and rearranging the indices, an FE equation can be derived in the form

$$\sum_{k=1}^{2M} g_{ik} I^e_k = r'_i, \qquad i = 1, \ldots, 2M \tag{7}$$

for each element. These sets of equations are assembled into a global FE equation system. The detailed formulation is given by Roux et al.[19]

The FE formulation of the heat conduction analysis is not explained here, but it is noted that the nodes and the trial functions for temperature distribution are the same as those in the radiation analysis.

For the given temperature distribution $T(x, t)$ at time t, the intensity distribution $I(x, \mu, t)$ is obtained. Then the conduction analysis is performed using the obtained intensity. In this analysis the divergence $\partial q_r / \partial x$ is calculated by the following equation, which is derived from Eqs. (1), (3), and (4):

$$\frac{\partial q_r}{\partial x} = 2\pi(1 - \omega) K_e \left[2n^2 I_b(T) - \sum_{l=1}^{M} w_l I(x, \mu_l)\right] \tag{8}$$

The Crank–Nicolson scheme is used in time integration. Because the combined system is nonlinear with respect to temperature, iteration is done at each time step to obtain a fully convergent solution. The criterion of convergence is

$$\left(\sum_{i=1}^{N} \left|T_i^{k-1} - T_i^k\right| \Big/ T_i^k\right) \Big/ N < 0.001$$

where i, k, and N denote the node number, the iteration step, and the number of nodes, respectively.

Numerical Examples

To illustrate the accuracy of the numerical method developed in this study, comparisons with published solutions[13–16] are presented in Tables 1 and 2 where $\xi = \lambda_s K_e^2 t/(\rho c)$, $\theta = T/T_1$, and $\nu = \lambda_s K_e/(4n^2 \sigma T_1^3)$ are the dimensionless time, dimensionless temperature, and the conduction-radiation parameter, respectively, and τ is the optical depth. τ_0 is the optical thickness of the slab. The initial temperature θ_0 is uniform, and for $\xi > 0$, the two boundary surfaces are maintained at specified temperatures of θ_1 and θ_2, respectively. In the calculation by present FE code, the number of nodes is $N = 101$ and $M = 12$ in x and μ coordinates, respectively, and the dimensionless time step $\Delta\xi = 0.0001$.

Table 1 shows the results for different wall reflectivity cases. Agreements are good. Detailed temperature distributions are compared in Table 2 for two different ω. As a whole, the present code predicts slightly lower temperatures, but the differences are not significant. Thus, the developed code is equivalent to the other methods within the presented comparisons.

Experimental Procedure

A series of experiments was conducted to examine the developed FE code. The experimental setup is shown in Fig. 1. The used

Table 2 Comparison of the transient temperature distribution at $\xi = 0.01$[a]

	$\omega = 0.9$		$\omega = 0.1$	
τ/τ_0	Tsai and Lin[13]	Present	Tsai and Lin[13]	Present
0	1	1	1	1
0.05	0.5167	0.5237	0.6206	0.6689
0.15	0.0948	0.0912	0.2778	0.2735
0.25	0.0542	0.0507	0.1785	0.1711
0.35	0.0466	0.0437	0.1284	0.1236
0.5	0.0372	0.0351	0.0817	0.0789
0.65	0.0291	0.0275	0.0534	0.0516
0.75	0.0242	0.0229	0.0406	0.0393
0.85	0.0194	0.0183	0.0308	0.0298
0.95	0.0114	0.0106	0.0179	0.0174
1	0	0	0	0

[a]Where $\tau_0 = 2$, $\theta_1 = 1$, $\theta_2 = 0$, $\theta_0 = 0$, $\nu = 0.01$, and $\epsilon_1 = \epsilon_2 = 1$.

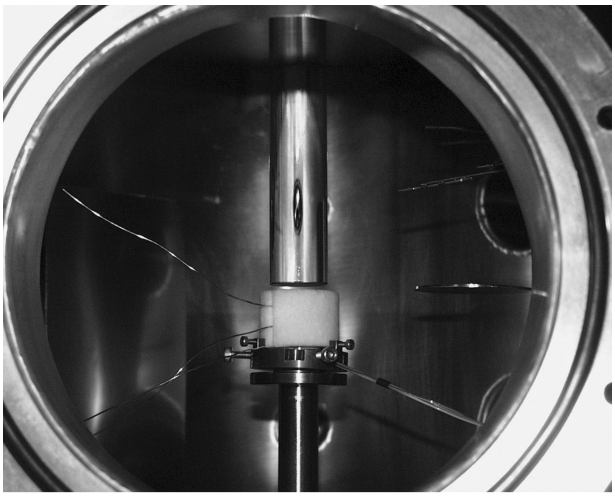

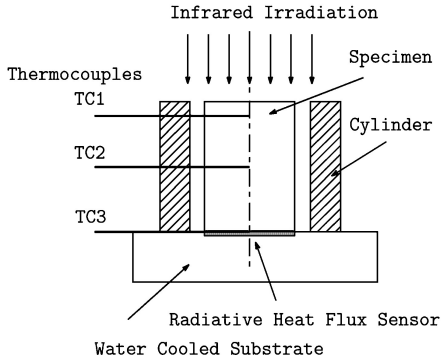

Fig. 1 Experimental setup.

material is a rigid ceramic tile insulation developed in the Japanese H-II Orbiting Plane-Experimental (HOPE-X) project. It is basically made of silica and alumina fibers, but further details are not publically available. The specimens were worked out from the tile. They are solid cylinders with diameter of 14 mm and thickness of $L = 5$, 15, 20, 30, and 40 mm. The axes of the specimens coincide with the out-of-plane direction of the tile.

The specimen was surrounded by a hollow cylindrical wall made of the same material intended to establish quasi-one-dimensional heat flow. This cylinder has an inner diameter of 18 mm, a thickness of 5 mm, and the same height as the specimen thickness. The specimen and the cylinder were placed on the water-cooled substrate. A thin radiative heat flux sensor (Captec Enterprise), whose diameter and thickness are 13 and 0.2 mm, respectively, was installed between the specimen and the substrate so that the radiative heat flux coming from the internal portion of the specimen was measured. The error of this radiative heat flux sensor is 5%. Three thermocouples (TCs) were used to measure the temperature at three different points along

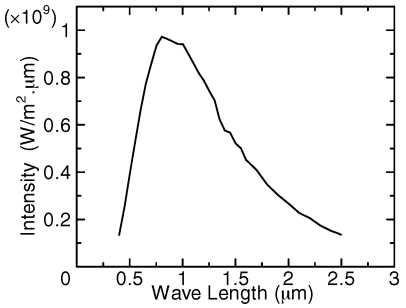

Fig. 2 Spectral intensity of infrared lamp.

the centerline of the specimen: 3 mm below front surface (TC1), middle (TC2), and back surface (TC3). R-type TCs with diameter of 0.3 mm were used for TC1 and TC2 and a K-type TC for TC3. Two holes with diameter of 0.3 mm and depth of 7 mm were very carefully made at the locations of TC1 and TC2. These two TCs were installed into these guide holes. The TC3 was built-in in the radiative heat flux sensor.

An infrared lamp was used for heating. Its spectral intensity is shown in Fig. 2. As shown in Fig. 1, infrared rays generated by the lamp are transported into the vacuum chamber through a solid glass rod with a diameter of 20 mm and are emitted from the bottom. This rod system realizes the concentrated high heat flux. The water-cooled substrate is movable with a digital scale so that one can locate the specimen with an accuracy of 0.01 mm. The distance between the bottom of the glass rod and the specimen front surface was set to be 3 mm in all tests, including the calibration explained later.

The magnitude of the infrared irradiation was measured by Thermogage flux sensor (Vatell Corp.) before the tests for calibration. According to the calibration data, the error in irradiation magnitude was less than 5% from the specified value.

All tests were conducted in the high-vacuum environment on the order of 0.1 mPa so that the effect of air was completely eliminated. The vacuum system is composed of a rotary pump and a turbomolecular pump. The vacuum chamber, whose diameter and height are 220 and 210 mm, respectively, is made of stainless steel. The reflection from the chamber wall was measured around the specimen under the actual heating conditions and was found to be negligible.

Using a shutter located 1 mm below the glass rod for heating, stepwise heat flux with the controlled magnitude of $Q_{ir} = 100$, 200, 300, and 400 kW/m^2 was imposed for 1200 s in all tests except $L = 5$ and 15 mm. In these thin-specimen cases, only the radiative heat flux was measured for several seconds to avoid overheating of the flux sensor. A period of natural cooling followed the heating for another 1200 s.

There can be large error in temperature measurement because of the large temperature gradient and the difficulty in placing the thermocouples at the exact position due to the brittle nature of the material. The holes for thermocouple installation were observed by a microscope after the tests. Then the error in location was estimated to be ± 0.3 mm. Next, using the radiation equilibrium temperature at the front surface and the measured temperature of TC1, the average temperature gradient was obtained. The error of TC1 was then estimated by multiplying the temperature gradient times the error in location. The error of TC2 was also estimated in the same way using the data of TC1 and TC2. It was found the maximum errors could occur in the case $L = 20$ mm, $Q_{ir} = 400$ kW/m^2. They were estimated to be ± 40 K for TC1 and ± 11 K for TC2. The temperature distribution can also be disturbed by thermocouples themselves, but it is not realistic to compensate for the disturbance in the measurement or to take into account the effect by three-dimensional fine modeling. Instead, to minimize the influence, the thinnest thermocouples were chosen, and the use of cement in measurement holes was avoided.

The imposed radiant flux distribution was measured by the Thermogage flux sensor. It was spatially uniform within at least 3 mm from the center. At the edge of the specimen, the flux decreased from the value at the center by 4, 8, 10, and 10% for $Q_{ir} = 100$, 200, 300,

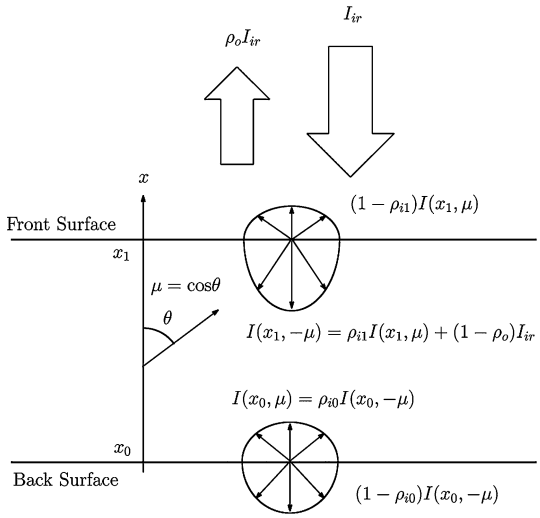

Fig. 3 Boundary conditions for radiative transfer equation.

and 400 kW/m^2, respectively. The effect of this flux-dependent distribution will be discussed in evaluating the radiation properties in the next section.

Experimental Results and Analysis

Boundary Conditions

Figure 3 shows the boundary conditions for radiation analysis. The coordinates of the back surface (bottom) and the front surface (heated surface) are $x = x_0$ and $x = x_1$, respectively, and the thickness of the specimen is L. No external irradiation is assumed at $x = x_0$ because the substrate is water cooled. The boundary conditions for the radiative transfer equation are given in the following equations with $\mu > 0$:

$$I(x_0, \mu) = \rho_{i0} I(x_0, -\mu)$$
$$I(x_1, -\mu) = \rho_{i1} I(x_1, \mu) + (1 - \rho_o) I_{ir} \tag{9}$$

where I_{ir} is the external irradiation intensity at the front surface. Because a diffuse surface is assumed, $I_{ir} = Q_{ir}/\pi$.

The boundary conditions for conduction equation are as usual. Surface radiative heat flux Q_{ir} is specified, and the emission from this hot surface is taken into account. The measured temperature T_0 by TC3 is used as the temperature boundary condition at the back surface.

Radiation Properties

Figures 4a–4d show the transient behaviors of radiative heat flux Q_r at the back surface. The typical time history of Q_r consists of three parts: instantaneous rise at the start of irradiation, gradual increase lasting about 200 s, and stationary state. The instantaneous rise Q_{r0} is observed in response to the stepwise irradiation Q_{ir} at $t = 0$. It indicates that a part of Q_{ir} reaches the back surface directly. As time elapses, temperature in the neighbor of the front surface increases, making not only the thermal conduction but also the inner radiation intense. The gradual increase of Q_r corresponds to this transient state. Finally, the temperature field reaches the steady state, and Q_r also becomes stationary.

Figure 5a shows the relationship between Q_{r0} and Q_{ir}. It is clear that Q_{r0} is proportional to Q_{ir}. Figure 5b shows the ratio Q_{r0}/Q_{ir} as a function of the specimen thickness L. An exponential relationship holds for the thicker specimens but does not for $L = 5$ and 15 mm. The ratio has a very high value for these thin specimens.

To investigate the theoretical background of Figs. 5a and 5b, the two-flux method is employed as follows. The self-absorption/emission is neglected at $t = 0$ because the temperature is still uniform and low (room temperature). Under the boundary conditions [Eq. (9)], the two-flux method yields the solution

$$Q_{r0} = g(L) Q_{ir} \tag{10}$$

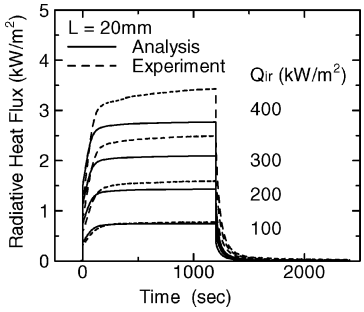

Fig. 4a Transient behaviors of radiative heat flux at the back surface, L = 20 mm.

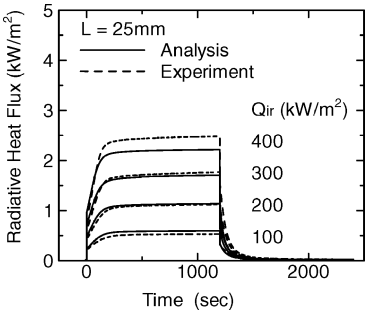

Fig. 4b Transient behaviors of radiative heat flux at the back surface, L = 25 mm.

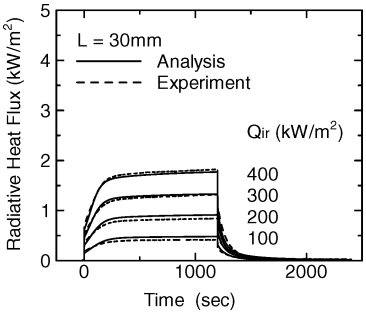

Fig. 4c Transient behaviors of radiative heat flux at the back surface, L = 30 mm.

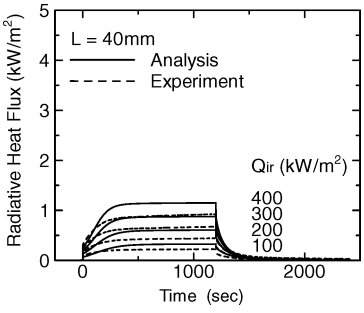

Fig. 4d Transient behaviors of radiative heat flux at the back surface, L = 40 mm.

where

$$g(L) = \frac{4(1-\rho_o)(1-\rho_{i0})\beta \exp(2K_e\beta L)}{A\exp(4K_e\beta L) - B}$$
$$A = 2(1+\beta) + \rho_{i0}\{\rho_{i1}(2-2\beta-\omega)-\omega\} - (1+\rho_{i1})\omega$$
$$B = 2(1-\beta) + \rho_{i0}\{\rho_{i1}(2+2\beta-\omega)-\omega\} - (1+\rho_{i1})\omega$$
$$\beta = \sqrt{1-\omega} \tag{11}$$

Equation (10) means that Q_{r0} is proportional to Q_{ir}, which coincides with the experimental results.

Table 3 Material constants

Constant	FEM	Two flux
ρ_o	0.85	0.86
ρ_{i0}	0	0
ρ_{i1}	0	0
K_e, m^{-1}	1.57×10^3	1.24×10^3
ω	0.999	0.999
n	1	——
ϵ	0.15	——
ρ, kg/m^3	100	——
c, $J/kg \cdot K$	691	——
λ_s, $W/m \cdot K$	0.03	——

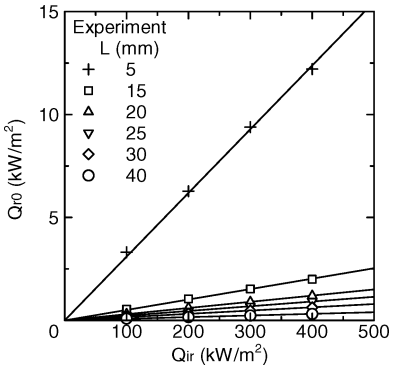

Fig. 5a Relationship between Q_{ir} and Q_{r0}.

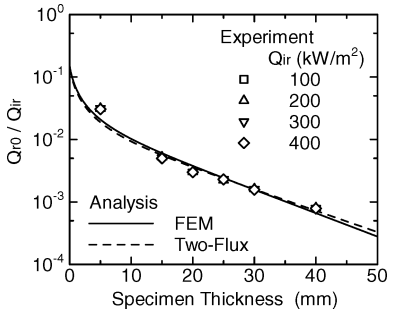

Fig. 5b Relationship between Q_{r0}/Q_{ir} and L.

As mentioned before, there is a flux-dependent spatial distribution in the surface incident. If this distribution had a significant effect, a nonlinear relationship between Q_{r0} and Q_{ir} would be observed in Fig. 5a. Indeed, a slight nonlinearity can be found for $L = 5$ mm, the thinnest specimen. It can be attributed to the incident flux distribution. However, the nonlinearity is not found in the thicker specimens. Thus, the effect of spatial distribution of radiant flux is not significant.

The ratio Q_{r0}/Q_{ir} can numerically be calculated by the developed FE code. Then a set of material constants regarding radiation, K_e, ω, ρ_{i0}, ρ_{i1} and ρ_o, were determined by minimizing the differences between calculated and measured Q_{r0}/Q_{ir}. The obtained values are shown in Table 3. Scattering is the dominant process in radiative transfer in ceramic tile insulation.[7] It indicates that ω is close to unity, which is consistent with the determined value. Both of the inner reflectivities ρ_{i0} and ρ_{i1} were determined to be zero. Note that Roux et al. assumed the same values in their analysis of fibrous insulation.[19] The calculated Q_{r0}/Q_{ir} is shown in Fig. 5b.

For a supplement, the material constants were also determined using Eq. (10). The determined values are shown in Table 3, and the function $g(L)$ obtained by Eq. (10) is shown in Fig. 5b. There are small differences between the values obtained by the FE method (FEM) and the two-flux method. One can find 21% difference in the extinction coefficient. This may be attributed to the simplified distribution of radiation intensity with respect to the polar angle in the two-flux method. However, they yield almost identical curves in Fig. 5b.

Results and Discussion

Radiation properties obtained by the FEM were used in the combined radiation–conduction analysis. Other material constants were determined as follows and are listed in Table 3. The refractive index was assumed to be unity. This assumption was also used by Marschall et al.[8] and by Daryabeigi,[11] in analyzing radiation transport through ceramic insulation and fibrous insulation, respectively, because in a high-porosity medium, the effective index of refraction should be dominated by the index of refraction of the void space.

The conductivity obtained by the GHP method at room temperature in a vacuum was used as the solid conductivity because the effects of air and radiation can be neglected in this condition. The value of the density was nominal. The specific heat was determined based on the transient behaviors in temperature response. All of the material properties were assumed to be constant for simplicity. The reasons for the simplification of the material properties are that the material details are not open to the public and no data of detailed properties are available.

To ensure the accuracy of the computation under the boundary conditions [Eq. (9)] and the determined material constants, test analyses were conducted with different mesh sizes Δx and time steps Δt for $L = 20$ mm and $Q_{ir} = 400$ kW/m^2. The calculated temperatures of TC2 (middle) at $t = 50$ s are listed in Table 4. It is found that the combination of $\Delta x = 0.2$ mm and $\Delta t = 0.01$ s is sufficient, and it was used in the following analyses.

Figures 4a–4d show the results of radiative heat flux Q_r at the back surface. An example of transient temperature response and the steady temperature distributions are shown in Figs. 6 and 7a–7d, respectively.

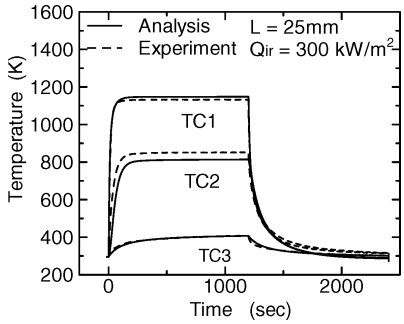

Fig. 6 Transient temperature response, L = 25 mm, Q_{ir} = 300 kW/m^2.

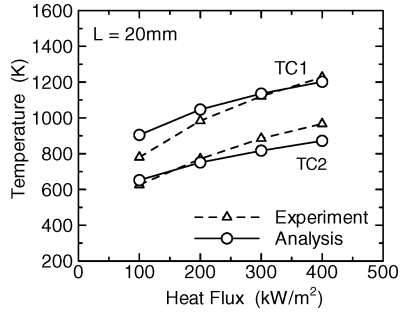

Fig. 7a Steady temperature distribution, L = 20 mm.

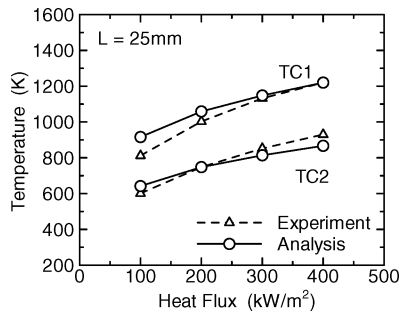

Fig. 7b Steady temperature distribution, L = 25 mm.

Table 4 Calculated temperature of TC2 degrees Kelvin with different mesh sizes and time steps

Time step	Mesh size Δx, mm				
Δt, s	2	1	0.5	0.2	0.1
0.005	6.886E+02	6.941E+02	6.954E+02	6.958E+02	6.958E+02
0.01	6.886E+02	6.941E+02	6.954E+02	6.958E+02	6.958E+02
0.02	6.885E+02	6.940E+02	6.953E+02	6.956E+02	6.957E+02

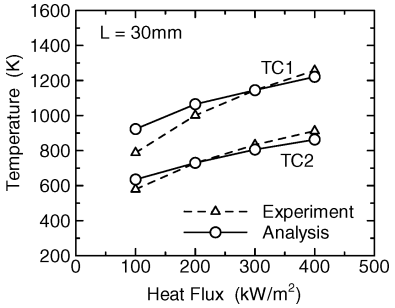

Fig. 7c Steady temperature distribution, L = 30 mm.

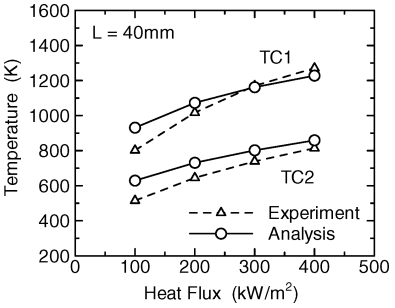

Fig. 7d Steady temperature distribution, L = 40 mm.

The analysis of the radiative heat flux at the back surface can be a good measure to examine the code because its behavior is a result of the combination of radiation and conduction in the material. Although differences are observed in some cases, good agreements are found as a whole in Figs. 4a–4d.

The calculated Q_r is low for the cases $L = 20$ mm with $Q_{ir} = 300$ and 400 kW/m^2 and $L = 25$ mm with $Q_{ir} = 400$ kW/m^2. These disagreements are correlated to the temperature predictions of TC2 (middle), where they are all lower than experimental data, as shown in Figs. 7a and 7b.

A quick rise in the back surface temperature (TC3), which is faster than expected under the assumption that only conduction occurs, is observed in Fig. 6. The reason for this may be that the specimen is thin and a part of Q_{ir} goes through the specimen to the back surface directly. Indeed, no instantaneous temperature rise was observed for $L = 40$ mm (the thickest specimen). In the case of Fig. 6 ($L = 25$ mm, $Q_{ir} = 300$ kW/m^2), 0.23% of the irradiated heat flux (690 W/m^2) reaches the back surface at the moment when heating starts.

In case of the thickest specimen, $L = 40$ mm, the experimental results of Q_r and temperature (especially TC2) are both lower than the analytical results. The discrepancies are more significant than with other specimens. This can be attributed to the heat loss from the side. Better predictions may be obtained by extending the present one-dimensional code to an axisymmetric or three-dimensional one.

Conclusions

An FE code was developed for combined radiation–conduction analysis, and its validity was discussed. Comparisons with published solutions showed that the developed code is equivalent to the other methods within the present study.

A series of experiments was conducted with a rigid ceramic insulation. The transient temperature distribution and the radiative heat flux at the back surface were measured. The radiative heat flux consists of three parts: instantaneous increase in response to the stepwise irradiation, gradual increase due to temperature rising, and stationary state. The analysis of this behavior can be a good measure to examine the code because it reflects the combination of radiation and conduction in the material. As a whole, good agreement was found between experimental data and analytical results.

Introducing more detailed material properties, such as anisotropy and temperature dependencies, is expected to improve the prediction. Also an extension to an axisymmetric or three-dimensional code should be done to make the analysis more realistic.

References

[1]Curry, D. M., and Williams, S. D., "Nonlinear Least Squares—An Aid to Thermal Property Determination," *AIAA Journal*, Vol. 11, No. 5, 1973, pp. 670–674.

[2]Williams, S. D., and Curry, D. M., "Effective Thermal Conductivity Determination for Low-Density Insulating Materials," NASA TP-1155, Feb. 1978.

[3]Banas, R. P., and Cunnington, G. R., Jr.,"Determination of Effective Thermal Conductivity for the Space Shuttle Orbiter's Reusable Surface Insulation (RSI)," AIAA Paper 74-730, July 1974.

[4]Williams, S. D., and Curry, D. M., "Prediction of Rigid Silica Based Insulation Conductivity," NASA TP-3276, Jan. 1993.

[5]Daryabeigi, K., "Analysis and Testing of High Temperature Fibrous Insulation for Reusable Launch Vehicles," AIAA Paper 99-1044, Jan. 1999.

[6]Zumbrunnen, D. A., Viskanta, R., and Incropera, F. P., "Heat Transfer Through Porous Solids with Complex Internal Geometries," *International Journal of Heat and Mass Transfer*, Vol. 29, No. 2, 1986, pp. 275–284.

[7]Schmitt, R. J., Linford, R. M. F., Dillow, C. F., and Hughes, T. A., "The Infrared Properties of Reusable Surface Insulations," AIAA Paper 73-745, July 1973.

[8]Marschall, J., Maddren, J., and Parks, J., "Internal Radiation Transport and Effective Thermal Conductivity of Fibrous Ceramic Insulation," AIAA Paper 2001-2822, June 2001.

[9]Tong, T. W., and Tien, C. L., "Radiative Heat Transfer in Fibrous Insulations—Part I: Analytical Study," *Journal of Heat Transfer*, Vol. 105, Feb. 1983, pp. 70–75.

[10]Tong, T. W., Yang, Q. S., and Tien, C. L., "Radiative Heat Transfer in Fibrous Insulations—Part II : Experimental Study," *Journal of Heat Transfer*, Vol. 105, Feb. 1983, pp. 76–81.

[11]Daryabeigi, K., "Heat Transfer in High-Temperature Fibrous Insulation," *Journal of Thermophysics and Heat Transfer*, Vol. 17, No. 1, 2003, pp. 10–20.

[12]Daryabeigi, K., "Thermal Analysis and Design Optimization of Multilayer Insulation for Reentry Aerodynamic Heating," *Journal of Spacecraft and Rockets*, Vol. 30, No. 4, 2002, pp. 509–514.

[13]Tsai, J-H., and Lin, J.-D., "Transient Combined Conduction and Radiation with Anisotropic Scattering," *Journal of Thermophysics*, Vol. 4, No. 1, 1990, pp. 92–97.

[14]Lii, C. C., and Ozisik, M. N., "Transient Radiation and Conduction in an Absorbing, Emitting and Scattering Slab with Reflective Boundaries," *International Journal of Heat and Mass Transfer*, Vol. 15, No. 5, 1972, pp. 1175–1179.

[15]Sutton, W. H., "A Short Time Solution for Coupled Conduction and Radiation in a Participating Slab Geometry," *Journal of Heat Transfer*, Vol. 108, No. 2, 1986, pp. 465–466.

[16]Barker, C., and Sutton, W. H., "The Transient Radiation and Conduction Heat Transfer in a Gray Participating Medium with Semi-Transparent Boundaries," *ASME Radiation Heat Transfer*, edited by B. F. Armaly and A. F. Emery, HTD-Vol. 49, American Society of Mechanical Engineers, Fairfield, NJ, 1985, pp. 25–36.

[17]Blosser, M. L., "Development of Metallic Thermal Protection Systems for the Reusable Launch Vehicle," NASA TM-110296, Oct. 1996.

[18]Cunnington, G. R., and Lee, S. C., "Radiative Properties of Fibrous Insulations: Theory Versus Experiment," *Journal of Thermophysics and Heat Transfer*, Vol. 10, No. 3, 1996, pp. 460–466.

[19]Roux, J. A., Yeh, H. Y., Smith, A. M., and Wang, S. Y., "Finite Element Analysis of Radiative Transport in Fibrous Insulation," *Journal of Energy*, Vol. 7, Nov.–Dec. 1983, pp. 702–709.